1128

JOURNAL OF MODERN OPTICS, 1996, VOL. 43, NO. 5, 1035–1053

Photonic band structure of guided Bloch modes in high index films fully etched through with periodic microstructure

D. M. ATKIN, P. ST. J. RUSSELL, T. A. BIRKS
Optoelectronics Research Centre, University of Southampton, Hampshire SO17 1BJ, England

and P. J. ROBERTS
Defence Research Agency, St. Andrews Road, Malvern WR14 3PS, England

(*Received 18 October 1995*)

Abstract. By adapting the well-known 'zigzag' ray model for use with a *periodic* waveguide (i.e. replacing the plane wave rays with Bloch wave rays), we show that thin films of high refractive index, supported by a low index substrate and fully etched through with a periodic pattern, can support guided modes. From the dispersion relation of these guided *Bloch* modes, it is shown that the in-plane modal group velocity can be zero, suggesting applications in enhanced dipole–field interactions and control of spontaneous emission in waveguide lasers.

1. Introduction

It is now accepted that, within a band of frequencies known as a photonic band gap (PBG), all the electromagnetic modes in a volume of dielectric material can be suppressed by appropriate periodic patterning, i.e. by the creation of a *photonic crystal* [1–3]. This permits a single intra-PBG electromagnetic mode (or resonance) with high quality factor (Q) to be introduced by means of a structural point defect. At the resonant frequency of this mode there can appear a substantial (depending on the Q-factor) enhancement in vacuum field intensity. If an electronic dipole whose transition coincides with this frequency is introduced, spontaneous emission will be enhanced and low threshold highly efficient lasing achieved [4].

The first such microlaser awaits the realization of a full PBG at optical frequencies, a task which pushes at the limits of what is possible in state-of-the-art nanofabrication. In the face of this considerable technological challenge, a number of groups worldwide are investigating the use of simpler structures supporting PBGs in two dimensions [5–10]. For example, arrays of closely spaced vertical cavity emitting lasers are being constructed in which it is hoped to suppress lateral emission by creating an in-plane PBG [11]. The performance of structures of this sort will, however, only be attractive if *waveguiding* is built into the designs, i.e. if fully trapped transverse resonances are created where the light bounces to and fro between the upper and lower interfaces of the periodic layer. Only a few of the published numerical studies of photonic band structure in two dimensions treat this case [6, 8, 12]. Most do not allow for propagation along the third dimension—essential if guided modes are sought.

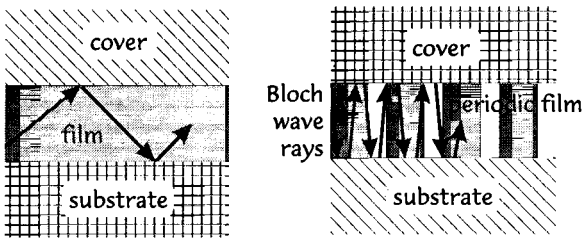

Figure 1. Comparison of (left) the conventional approach to tackling propagation in a weakly periodic guide and (right) the approach adopted in this paper in which the Bloch waves of the periodic layer are used to construct the guided Bloch modes.

Prior analyses on Bragg diffraction in periodic waveguides (e.g. fibre gratings or DFB lasers) start with the assumption that the refractive index modulation is weaker than the index step that forms the waveguide [13]. This allows one to construct a theory based on the coupling of power between a pair of guided modes satisfying a Bragg condition, the essential approximation being that the 'strongly' guided modes are resistant to the weaker periodic perturbation. In this paper, driven by the PBG requirement for large index modulation, we tackle the case (see figure 1) where this is no longer a good approximation. Rather than building *coupled mode equations* from the *guided modes* of a film of the same average index, we construct the *guided modes* of the fully etched layer from the *Bloch waves* of the periodic medium out of which the layer is constructed. The resulting *guided Bloch modes* contain all the salient features of propagation in the periodic layer, including the photonic band structure, dispersion and group velocity. As we shall show, stationary modes can be found (at particular frequencies) that have zero group velocity in the guiding plane. These modes will interact very strongly with a dipole of the correct frequency if it is incorporated into the waveguide.

The generic structure (figure 2) consists of strips of high index dielectric sandwiched between media of lower refractive index, the cover and the gaps between the strips being air. This provides an extremely high modulation depth of the refractive index in-plane. Although there are physical gaps in the wave-guiding layer, these turn out—under the correct conditions—to be below the resolution limit of light both in the cover and the substrate, permitting strongly guided modes to be supported. We shall now obtain the field structure and

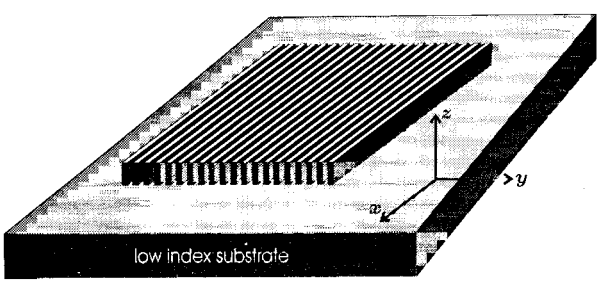

Figure 2. The structure analysed consists of lines of high refractive index placed on a substrate of low refractive index, the other regions being filled with air. Propagation in the (y, z) plane only is considered.

dispersion of the Bloch modes in an infinite periodic stack, and then use a 'zigzag' ray picture [14] (in which the ray direction is given by the group velocity of the Bloch waves) to derive the dispersion relation of the guided Bloch modes in a slice of this stack placed between two media of lower refractive index.

2. Bloch waves of infinite periodic stack

Our starting point is the standard translation matrix technique for a dielectric stack formed from alternating layers of high and low refractive index [9, 15]. We use this to obtain the dispersion relation for the Bloch waves. For completeness we present the main steps in this analysis, relegating most of the details to the Appendix.

The dielectric stack consists of alternating layers of refractive index n_1 and n_2 and widths h_1 and h_2 the stack period being $\Lambda = (h_1 + h_2)$. Cartesian axes are oriented with y normal to the layer boundaries and z along the layers (figure 2). No field variation with x is allowed, which allows separation of the fields into transverse magnetic (TM) and transverse electric (TE) states, with respectively $E_x = H_y = H_z = 0$ and $H_x = E_y = E_z = 0$. In each case, all field components can be written in terms of the surviving x-component, f, which may be expressed in the jth layer ($j = 1, 2$) of the Nth period as:

$$f_j^N(y) = a_j^N \cos\left[p_j(y - y_j^N)\right] + b_j^N \frac{\sin\left[p_j(y - y_j^N)\right]}{\xi_j p_j \Lambda} \tag{1}$$

where a_j^N and b_j^N are constants to be determined, y_j^N is the value of y at the centre of the jth layer of the Nth period and p_j is the wavevector component of the field normal to the interface within each medium:

$$p_j = (k^2 n_j^2 - \beta^2)^{1/2} \tag{2}$$

where β is the propagation constant in the z direction and $\mathbf{k}$ is the vacuum wavevector. The TE and TM cases are selected via the parameter ξ_j:

$$\xi_j = 1 \quad \text{(TE)} \qquad \text{or} \qquad \xi_j = 1/n_j^2 \quad \text{(TM)}. \tag{3}$$

The field throughout the stack is completely specified by a two-component state vector consisting of the constants a_j^N and b_j^N. The state vector in one layer is related to the state vector in the corresponding layer in the previous period by operation with a 2×2 translation matrix, $\mathbf{M}$:

$$\begin{pmatrix} a_j^{N+1} \\ b_j^{N+1} \end{pmatrix} = \mathbf{M}\begin{pmatrix} a_j^N \\ b_j^N \end{pmatrix} = \begin{pmatrix} A & B \\ C & A \end{pmatrix}\begin{pmatrix} a_j^N \\ b_j^N \end{pmatrix}. \tag{4}$$

See the appendix for the elements of $\mathbf{M}$, and for the elements of the matrix $\mathbf{M}_{12}$ relating the state vector in layer $j = 1$ to the state vector in the neighbouring layer $j = 2$. The eigenvalues and eigenvectors of $\mathbf{M}$ are given simply by:

$$\lambda_\pm = A \pm (BC)^{1/2}, \qquad \mathbf{f}_\pm = \begin{pmatrix} +B^{1/2} \\ \pm C^{1/2} \end{pmatrix} \tag{5}$$

where $BC = A^2 - 1$ and $|\mathbf{M}| = 1$, i.e. $\mathbf{M}$ is unimodular. This implies that the product of the eigenvalues is unity and thus, without loss of generality, that:

$$\lambda_{\pm} = \exp(\pm \mathrm{j} k_y \Lambda), \quad k_y = \frac{\arccos A}{\Lambda} \tag{6}$$

where k_y is the Bloch wavevector. For a given polarization state at fixed optical frequency and β, the complete field in the structure is expressible as a superposition of two Bloch waves with field distributions:

$$f_{\pm}(y) \exp[-\mathrm{j}\beta z] = B_{\pm}(y) \exp[-\mathrm{j}(\beta z \pm k_y y)] \tag{7}$$

where the function $B_{\pm}(y)$ is periodic with period Λ.

3. The wavevector diagram

The wavevector diagram is a plot of the loci of real wavevectors at fixed optical frequency in the multilayer stack. It is extremely useful for establishing a clear graphical understanding of the boundary conditions on either side of the periodic layer [9]. First the following set of normalized parameters is adopted:

$$\begin{gathered} n_{\mathrm{av}} = (n_1 h_1 + n_2 h_2)/\Lambda \\ \nu = k n_{\mathrm{av}} \Lambda, \quad n_{\mathrm{R}} = n_2/n_1, \quad \tau = h_2/\Lambda \end{gathered} \tag{8}$$

where n_{av} is the *weighted average index*, ν is the *normalized frequency*, n_{R} the *index ratio* and τ the *relative layer thickness*. A series of wavevector diagrams, plotted for a multilayer structure consisting of alternating layers of air and silicon ($n_{\mathrm{R}} = 3{\cdot}45$) with $\tau = 0{\cdot}8$, is given in figure 3. For a normalized frequency $\nu = 2$ and TE propagation, the mode index of the Bloch waves is approximately isotropic and equal to the average index, n_{av}. The circles repeat in the y direction at intervals of $2\pi/\Lambda$ as a consequence of Bloch's theorem. The TM wavevector diagram on the other hand is elliptical, expressing the birefringence of the periodic structure. At a normalized frequency of $\nu = 3$ a momentum gap appears within a certain range of β values. In this gap the Bloch waves are evanescent, i.e. if the stack is infinite in extent they cannot exist. The group velocity of the travelling Bloch waves is given by:

$$\mathbf{v}_{\mathrm{g}} = \nabla_{\mathbf{k}} \omega(\mathbf{k}) \tag{9}$$

which indicates that $\mathbf{v}_{\mathrm{g}}$ is oriented normal to the curves in wavevector space, pointing in the direction of increasing frequency. The points where the momentum gap is narrowest occur at $k_y \Lambda/\pi = 1$, and will be referred to as the *symmetric points*; at these points the group velocity points exactly *along* the layers. When the normalized frequency is increased to 4, ellipse-like shapes appear in the momentum gaps. These give rise to an additional pair of symmetric points. We shall refer to the Bloch waves on the 'ellipse' as the fast Bloch waves and those on the outer branches as slow Bloch waves, a naming convention which relates to the phase velocity along the layers.

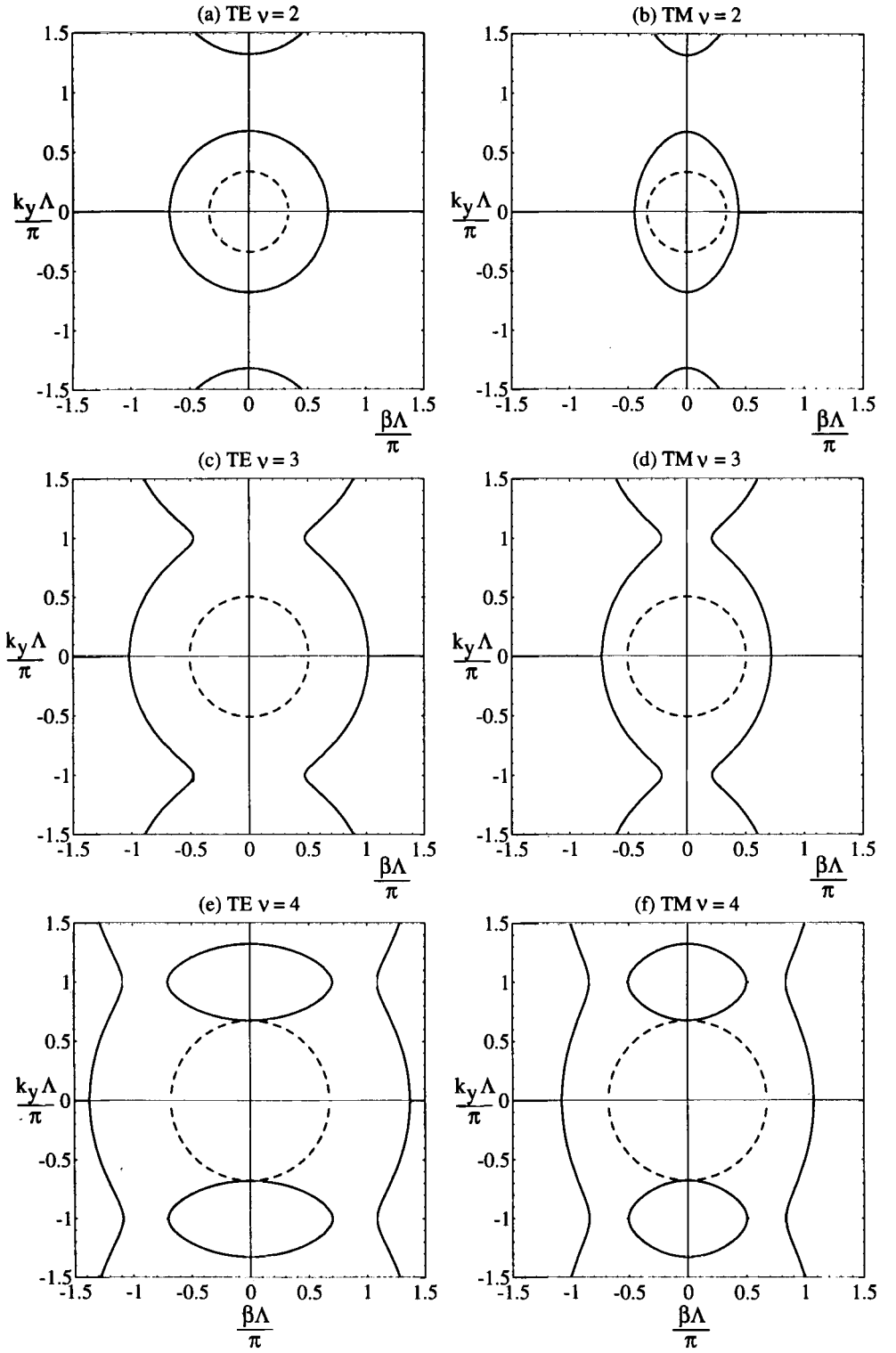

Figure 3. Series of wavevector diagrams for TE and TM cases at three different normalized frequencies ν in a multilayer stack with $n_1 = 1$, $n_2 = 3{\cdot}45$, $n_{ss} = 1{\cdot}57$, $n_{co} = 1$ and $\tau = 0{\cdot}8$.

4. Boundary conditions

At fixed optical frequency, boundary conditions specify that the components of wave momentum along a planar interface must be conserved as the interface is crossed. By superimposing the wavevector diagrams for the two adjoining materials, fulfilment of this condition is easy to visualize graphically. In our case the diagram for the substrate is simply a circle:

$$k_y^2 + \beta^2 = k^2 n_{ss}^2 = \left(\frac{n_{ss}\nu}{n_{av}\Lambda}\right)^2 \tag{10}$$

which is shown (with dotted curves) on figure 3. To treat phase matching at, for example, an interface in the (x, y) plane, a horizontal construction line is drawn on the (β, k_y) diagram. For $k_y\Lambda/\pi$ close to 1 this line does not intersect the substrate circle, so that total internal reflection occurs and the Bloch waves are trapped in the periodic layer. As $k_y\Lambda/\pi$ decreases, the line eventually intersects the substrate circle, and the Bloch waves radiate from the periodic layer into the substrate.

5. Symmetrical points on the frequency versus β diagram

On this diagram (figure 4), the positions of the momentum gap edges are plotted as a function of frequency for the same structure as treated in figure 3. In the regions of the diagram that are not shaded k_y is real and the corresponding Bloch waves propagate freely in the structure. Below the $k_y\Lambda/\pi = 0$ line the Bloch waves are cut-off. In the shaded regions between the $k_y\Lambda/\pi = 1$ lines, k_y is complex and the Bloch waves are evanescent. In the TM case the gap width shrinks to zero at $\beta\Lambda/\pi \approx 0{\cdot}3$, which occurs when the rays in each layer are incident on the interfaces at Brewster's angle.

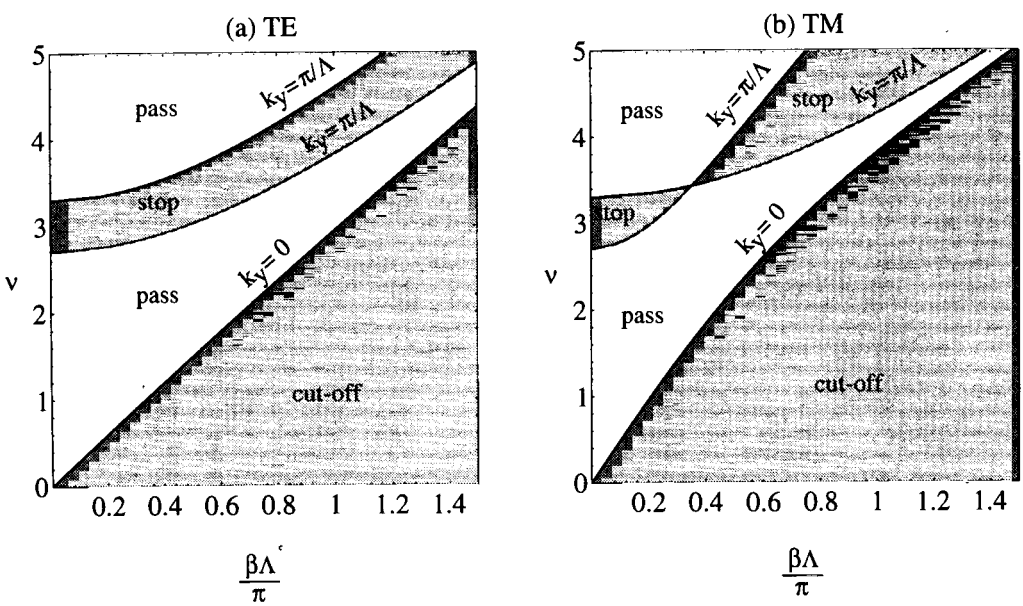

Figure 4. Frequency versus β diagram for the multilayer stack of figure 3 ($n_1 = 1$, $n_2 = 3{\cdot}45$, $n_{ss} = 1{\cdot}57$, $n_{co} = 1$ and $\tau = 0{\cdot}8$).

6. Two-wave approximation for the Bloch waves

To reduce the complexity of the problem, we now take the Fourier transform of the periodic part $B_{\pm}(y)$ of the Bloch wave fields, and extract the amplitudes of the *two dominant partial waves* in the plane-wave expansion. These are then matched to the fields with *upward* $(+y)$ and *downward* $(-y)$ progressing phase velocities (evanescent in the z-direction) in the substrate and cover regions. All the higher order partial plane waves are ignored; as we shall show, the accuracy of this approximation is such that the solutions compare favourably with the results of a numerical finite-difference analysis.

Each Bloch wave can be expanded in terms of an infinite set of partial plane waves whose wavevectors are related by Floquet's theorem:

$$k_n = \beta\hat{\mathbf{z}} + (k_y + nK)\hat{\mathbf{y}} \tag{11}$$

where $K = 2\pi/\Lambda$ is the grating vector. This permits us to express the exact solutions from the translation matrix analysis, $B_{\pm}(y)$ in (7), in the general form:

$$B_{\pm}(y) = \sum_n S_n^{\pm} \exp(-\mathrm{j}nKy) \tag{12}$$

where the $S_n^{\pm}$ are the complex plane wave amplitudes, whose values are easily found by performing Fourier analysis, yielding:

$$S_{\mathrm{n}}^{\pm} = \frac{1}{\Lambda}\int_{-\Lambda/2}^{\Lambda/2} B_{\pm}(y) \exp(\mathrm{j}nKy)\,\mathrm{d}y. \tag{13}$$

Retaining the two dominant partial waves, the Bloch wave fields $b_{\pm}(y, z)$ are given approximately by:

$$b_{\pm}(y, z) \approx \exp[-\mathrm{j}(\beta z \pm k_y y)](S_0^{\pm} + S_{-1}^{\pm} \exp(\mathrm{j}Ky)) \tag{14}$$

where as before the choice of $+$ or $-$ determines the group of Bloch waves that progresses (or evanesces) in the $+y$ or $-y$ directions.

The percentage errors in amplitude and phase introduced by this approximation are plotted in figure 5 for normalized frequencies of 3 and 4. For slow Bloch waves the amplitude error is less than 3% and the phase error less than 0·5% over the parameter range of interest. For fast Bloch waves the worst case is at the top of the frequency range and gives an amplitude error between 6 and 7% and a phase error less than 0·8%.

7. Guided Bloch modes

We are now in a position to obtain the dispersion relation of the guided Bloch modes. The interfaces are considered to be parallel and separated by a distance h. The boundary conditions require that all wavevector components in the y-direction be continuous across the interfaces. The most general case (or four participating Bloch waves) is illustrated in figure 6, the arrows indicating the directions of the group velocities in the layer. The upward (U) and downward (D) partial waves in each of the four Bloch waves (labelled by f (fast) and s (slow) for $\beta > 0$, and $\bar{\mathrm{f}}$ (fast) and $\bar{\mathrm{s}}$ (slow) for $\beta < 0$) are now matched to the upward and downward evanescent waves in the cover (co) and substrate (ss). The surviving x components b_{f}, $b_{\bar{\mathrm{f}}}$, b_{s}

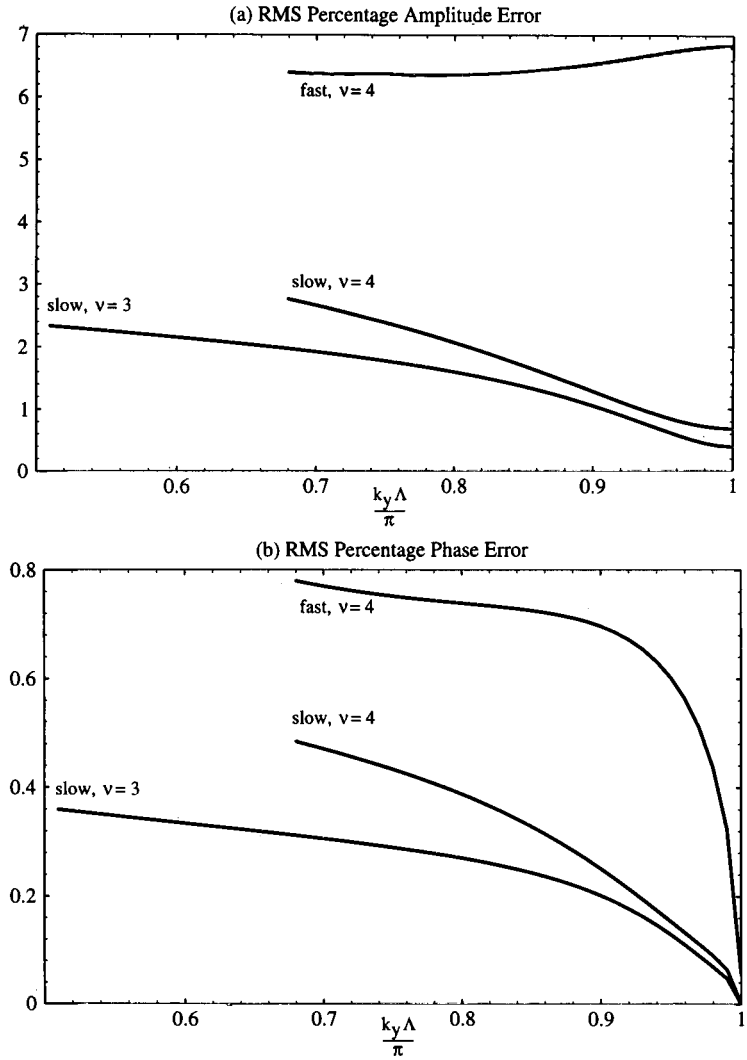

Figure 5. Percentage root mean square errors in (*a*) phase and (*b*) field amplitude introduced by truncation of the plane wave spectrum to two partial waves. The mean is averaged over one grating period ($n_1 = 1$, $n_2 = 3{\cdot}45$, $n_{ss} = 1{\cdot}57$, $n_{co} = 1$ and $\tau = 0{\cdot}8$). At a normalized frequency of 3 only slow waves exist and the errors are less severe. The size of the errors increase with increasing frequency. The errors for fast and slow waves are shown for the highest frequency of interest, $\nu = 4$.

and $b_{\bar{s}}$ of the Bloch wave fields (from (14), taking without loss of generality the + sign and replacing the subscripts $\pm$ with f or s) are:

$$\frac{b_f}{V_f \exp(-j\beta_f z)} = \frac{b_{\bar{f}}}{V_{\bar{f}} \exp(j\beta_f z)} = \exp(-jk_y y)(F_U + F_D \exp(jKy)) \qquad (15)$$

where f and F are simply replaced by s and S for the slow Bloch waves. The F_U and F_D are the renamed upward and downward partial wave amplitudes (identical for $\beta = \pm|\beta|$) from (14), β_f is the value of β on the inner (fast) stop-band branch,

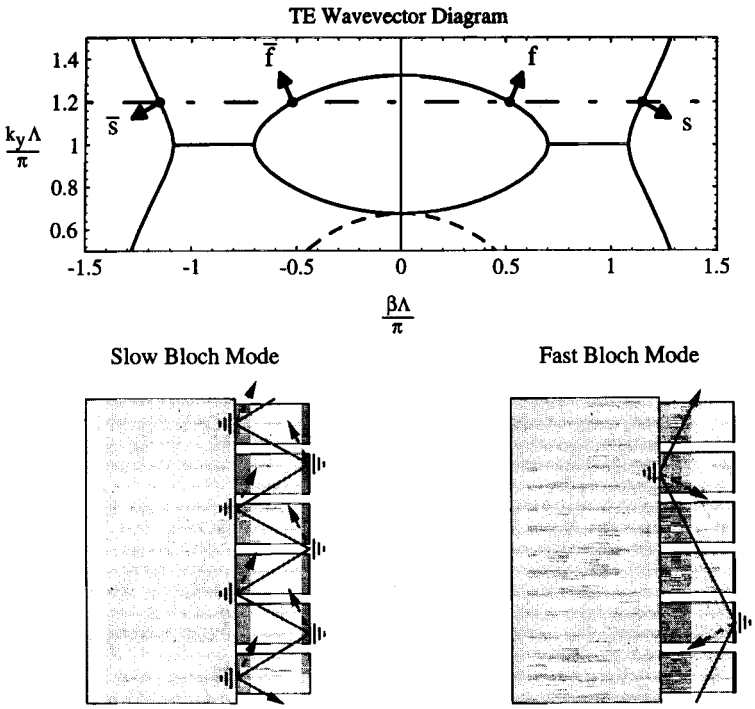

Figure 6. The waveguide modes are found by matching k_y at the substrate and air interfaces and then satisfying a resonance condition. At each interface four Bloch waves are matched to two evanescent plane waves, i.e. an incident wave of one type scatters partially into a wave of the other type at the interface. However only the waves that satisfy the resonance condition will propagate along the waveguide.

β_s is the value of β on the outer (slow) stop-band branch and V_j are the Bloch wave amplitudes (to be determined). If the 'ellipse' is not present, then β_f is pure imaginary. The Evanescent fields in the cover (E_{co}, $z \geqslant h/2$) and substrate (E_{ss}, $z \leqslant -h/2$) regions are given by:

$$E_{co} \exp(jk_y y) = U_{co} \exp[-(k_y^2 - k^2 n_{co}^2)^{1/2}(z - h/2)] + D_{co} \exp[-[(k_y - K)^2 - k^2 n_{co}^2]^{1/2}(z - h/2)] \exp(jKy)$$

$$E_{ss} \exp(jk_y y) = U_{ss} \exp[(k_y^2 - k^2 n_{ss}^2)^{1/2}(z + h/2)] + D_{ss} \exp[[(k_y - K)^2 - k^2 n_{ss}^2]^{1/2}(z + h/2)] \exp(jKy) \qquad (16)$$

where h is the layer width, U_{co}, U_{ss}, D_{co}, and D_{ss} being the upward ($+y$) and downward ($-y$) progressing wave amplitudes in the cover and substrate. Requiring continuity of the x-components and derivatives† of the upward and downward fields

† For the TM case the boundary condition, at the interface between the periodic structure and the cover or substrate, requies continuity of $(1/n^2(y))(dH_x/dz)$. In the present analysis it is assumed that, for this boundary condition, $n(y)$ is constant and equal to the average index, n_{av}. A more accurate approach would involve finding Fourier components of $1/n^2(y)$ and incorporating these into the analysis. However, when the results from both methods are compared, the error is very small, validating the initial approximation.

at the substrate and cover interfaces yields eight boundary conditions, which are most conveniently written in the form of a matrix equation:

$$\begin{pmatrix} F_U e^{+\phi} & F_U e^{-\phi} & S_U e^{-\sigma} & S_U e^{+\sigma} & -1 & 0 & 0 & 0 \\ F_D e^{+\phi} & F_D e^{-\phi} & S_D e^{-\sigma} & S_D e^{+\sigma} & 0 & -1 & 0 & 0 \\ F_U e^{-\phi} & F_U e^{+\phi} & S_U e^{+\sigma} & S_U e^{-\sigma} & 0 & 0 & -1 & 0 \\ F_D e^{-\phi} & F_D e^{+\phi} & S_D e^{+\sigma} & S_D e^{-\sigma} & 0 & 0 & 0 & -1 \\ \beta_f F_U e^{+\phi} & -\beta_f F_U e^{-\phi} & -\beta_s S_U e^{-\sigma} & \beta_s S_U e^{+\sigma} & -jp_{ssU} & 0 & 0 & 0 \\ \beta_f F_D e^{+\phi} & -\beta_f F_D e^{-\phi} & -\beta_s S_D e^{-\sigma} & \beta_s S_D e^{+\sigma} & 0 & -jp_{ssD} & 0 & 0 \\ \beta_f F_U e^{-\phi} & -\beta_f F_U e^{+\phi} & -\beta_s S_U e^{+\sigma} & \beta_s S_U e^{-\sigma} & 0 & 0 & jp_{coU} & 0 \\ \beta_f F_D e^{-\phi} & -\beta_f F_D e^{+\phi} & -\beta_s S_D e^{+\sigma} & \beta_s S_D e^{-\sigma} & 0 & 0 & 0 & jp_{coD} \end{pmatrix}$$

$$\times \begin{pmatrix} V_f \\ V_{\bar{f}} \\ V_s \\ V_{\bar{s}} \\ U_{ss} \\ D_{ss} \\ U_{co} \\ D_{co} \end{pmatrix} = \mathbf{0} \tag{17}$$

where

$$\phi = j\beta_f h/2, \qquad \sigma = j\beta_s h/2,$$
$$p_{jU} = \xi_j(k_y^2 - k^2 n_j^2)^{1/2}, \quad p_{jD} = \xi_j[(k_y - K)^2 - k^2 n_j^2]^{1/2}, \tag{18}$$
$$\xi_j = 1 \quad \text{(TE)} \quad \text{or} \quad \xi_j = n_{av}^2/n_j^2 \quad \text{(TM)}$$

are the definitions of the various parameters and j = co or ss. Real values of k_y for which the determinant of this matrix is zero yield the guided Bloch modes of the periodic layer. At the symmetric points ($k_y \Lambda/\pi = \pm 1$), the upward and downward partial waves have equal and opposite wavevectors, which means that the conditions for the upward and downward waves are identical. Since the fast and slow guided Bloch modes are orthogonal at this point and can be considered separately, the problem reduces to a much simpler 4 × 4 matrix yielding the following dispersion equation for the guided modes:

$$\tan(\beta_q h + m\pi) = \frac{\beta_q(p_{ssU} + p_{coU})}{\beta_q^2 - p_{ssU}p_{coU}} = \frac{\beta_q(p_{ssD} + p_{coD})}{\beta_q^2 - p_{ssD}p_{coD}} \tag{19}$$

where q = f or s (for the fast or slow Bloch waves) and m is an integer. This is very similar to the standard dispersion relation for an asymmetric slab waveguide [14].

8. Results

8.1. *Guided Bloch modes at symmetric points*

Figure 7 shows plots of normalized frequency v versus h/Λ for a Si structure on a glass substrate ($n_1 = 1$, $n_2 = 3{\cdot}45$, $n_{ss} = 1{\cdot}57$, $n_{co} = 1$, $\tau = 0{\cdot}8$, yielding $n_{av} = 2{\cdot}96$). Since they reside at the symmetrical points on the wavevector diagram, these guided Bloch modes have zero group velocity in the direction parallel to the substrate and are fully confined within the layer. For small values of h the modes are widely spaced in frequency. The upper set of curves (dashed line style) is for

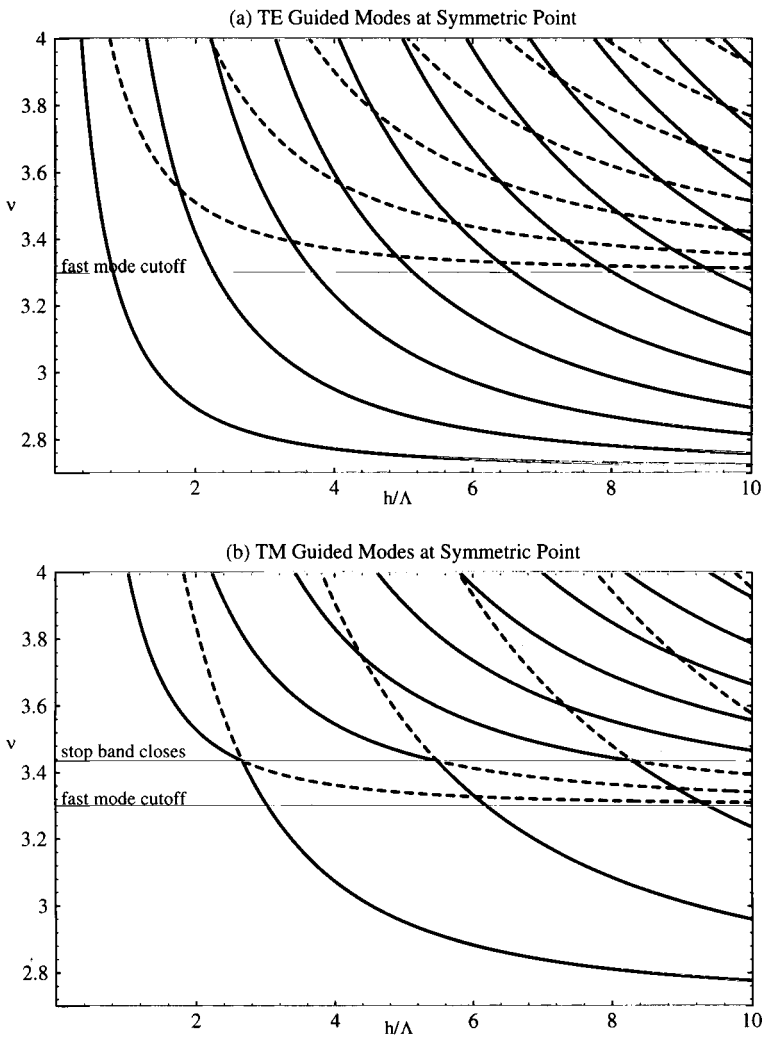

Figure 7. Normalised frequency v versus h/Λ for the guided Bloch modes at the symmetrical points in a Si structure on a glass substrate ($n_1 = 1$, $n_2 = 3{\cdot}45$, $n_{ss} = 1{\cdot}57$, $n_{co} = 1$ and $\tau = 0{\cdot}8$). The solid lines represent slow modes and the dashed lines represent fast modes. The fast mode cutoff at $v = 3{\cdot}2996$. In the TM case (b) the modes switch from fast to slow at $v = 3{\cdot}435$. This is a result of the definition of fast and slow modes and the crossing of the $k_y = \pi/\Lambda$ lines in figure 4 where the stop band closes.

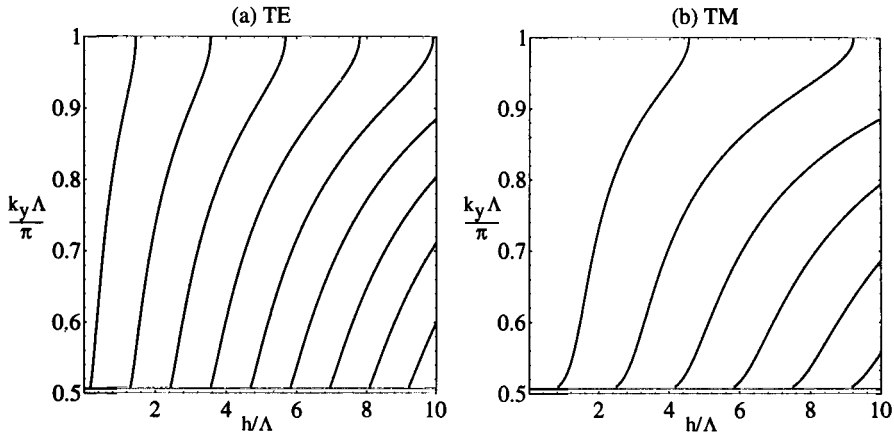

Figure 8. Plots of $k_y\Lambda/\pi$ versus normalized layer thickness h/Λ for (*a*) TE and (*b*) TM modes in a structure with $n_1 = 1$, $n_2 = 3{\cdot}45$, $n_{ss} = 1{\cdot}57$, $n_{co} = 1$ and $\tau = 0{\cdot}8$ at a normalized frequency $v = 3$. The fast modes are evanescent, and the slow modes cut off when the $k_y\Lambda/\pi$ intersects with the substrate circle.

the fast modes. These disappear at normalized frequencies below $v = 3{\cdot}2996$, which corresponds to the disappearance of the 'ellipse' on the wavevector diagram. The lower set of curves (full line style) is for the slow modes. The fast and slow modes occur in pairs, each pair straddling the corresponding mode that would occur in a homogeneous slab waveguide of the same average index.

8.2. *Behaviour away from symmetric points*

Away from the symmetric points, the guided Bloch modes are described by full solutions of (17). Plots of $k_y\Lambda/\pi$ versus normalized layer thickness h/Λ are presented in figure 8 for TE and TM modes at a normalized frequency $v = 3$. At this frequency only slow modes exist, there being no 'ellipse' on the wavevector diagram, rendering the fast modes evanescent. Note that for small enough layer thickness only one mode is available over the whole range of k_y. The guided modes cut off when $k_y\Lambda/\pi$ intersects with the substrate circle; this condition is indicated by the horizontal line near the base of the figures.

Figure 9 is a repeat of figure 8 for a normalized frequency $v = 4$. The set of near-vertical curves corresponds to slow modes, and the second set of curves corresponds to fast modes. As the modes move away from the symmetrical point, increasingly strong anti-crossing occurs at the intersection points of the curves. This is due to coupling between fast and slow Bloch waves at the interfaces. When, for example, a fast Bloch wave collides with the cover or substrate interface, it is split by total internal reflection into a mixture of a strong fast and a weaker slow Bloch wave.

8.3. *Brillouin diagram*

Figure 10 shows plots of v versus $k_y\Lambda/\pi$ for TE modes for a structure of thickness $1{\cdot}5\Lambda$ ($n_1 = 1$, $n_2 = 3{\cdot}45$, $n_{ss} = 1{\cdot}57$, $n_{co} = 1$ and $\tau = 0{\cdot}8$). The shaded regions to the upper left and right occur when $k_y\Lambda/\pi = vn_{av}$, i.e. when the substrate circle is touched and there is radiation into the substrate. The lowest curve with

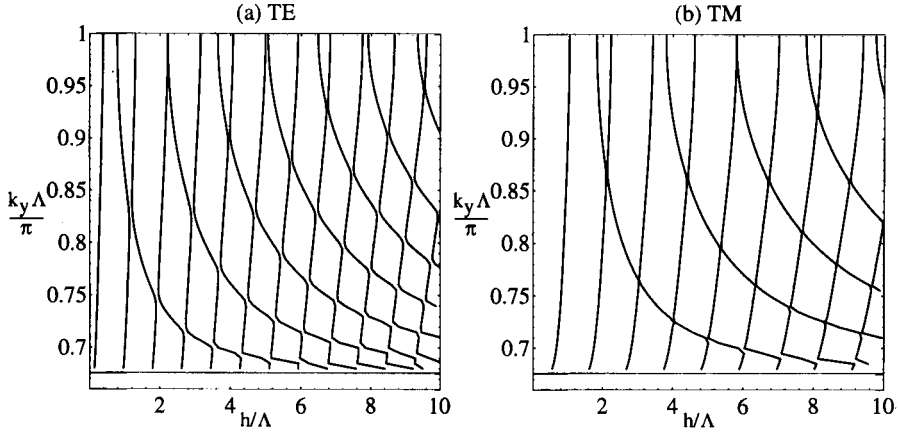

Figure 9. Plots of $k_y\Lambda/\pi$ versus normalized layer thickness h/Λ for (*a*) TE and (*b*) TM modes in the same structure as in figure 8, at a normalized frequency $v = 4$. Both fast and slow modes are present, and once again they cut off when the $k_y\Lambda/\pi$ intersects the substrate circle.

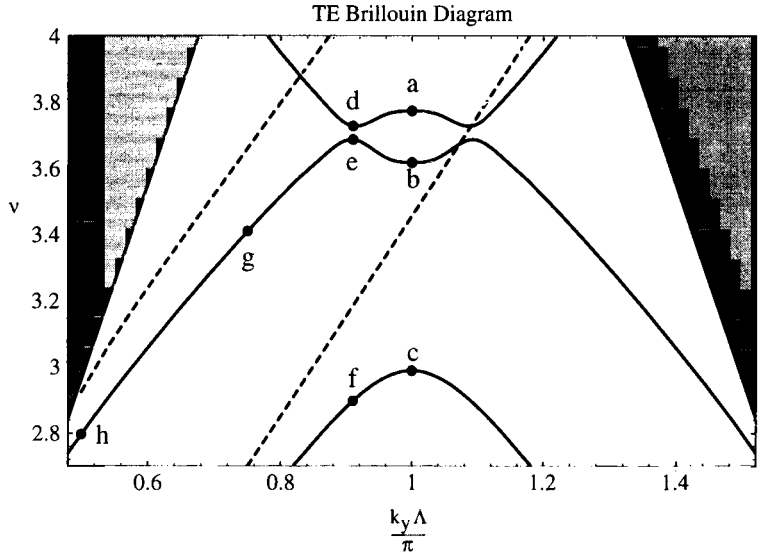

Figure 10. TE Brillouin diagram (v versus $k_y\Lambda/\pi$) for a structure of thickness $1{\cdot}5\Lambda$ ($n_1 = 1$, $n_2 = 3{\cdot}45$, $n_{ss} = 1{\cdot}57$, $n_{co} = 1$ and $\tau = 0{\cdot}8$). The shaded regions correspond to modes that radiate into the substrate. The solid curves are the Bloch wave modes and the dashed curves represent the zero and first order modes in a homogeneous waveguide with index $n_{av} = 2{\cdot}96$. The reference points are marked for table 1 and the field microstructure plots in figure 11.

the point c marked on it corresponds to the zero order slow Bloch wave mode. At points a, b, c, d and e the group velocity of the Bloch wave is zero in the y direction. The vanishingly small group velocity at the symmetric points will result in an enhancement in the interaction between the electromagnetic guided mode and an incorporated dipole of the same frequency. An excitation of finite length will contain a range of frequencies, with a decay time dependent on the bandwidth;

energy will leak away via guided Bloch modes that do not lie precisely on the symmetrical points (see section 9.2). The other two curves on the diagram represent the first order slow mode and the zero order fast mode. Between the points d and e the modes display an anticrossing behaviour. At points a, g and h the mode consists solely of the first order slow mode; at point b there is the zero order fast mode; finally at points d and e there is a mixture of the two modes. This is confirmed by the field microstructure in the next section. An intriguing feature of these plots is the *reduction* in the number of guided modes as the frequency rises. This is the reverse of the behaviour in normal waveguides, where higher frequencies imply a larger number of modes, and is caused by the encroachment of the momentum gap within the permitted range of β values. The modes in a homogeneous waveguide with the same average index are shown as dashed lines on the diagram. In the periodic structure the zero order mode is suppressed between points b and c, and the first order mode is suppressed above a. In thicker layers this mode-suppression effect is even more dramatic [16].

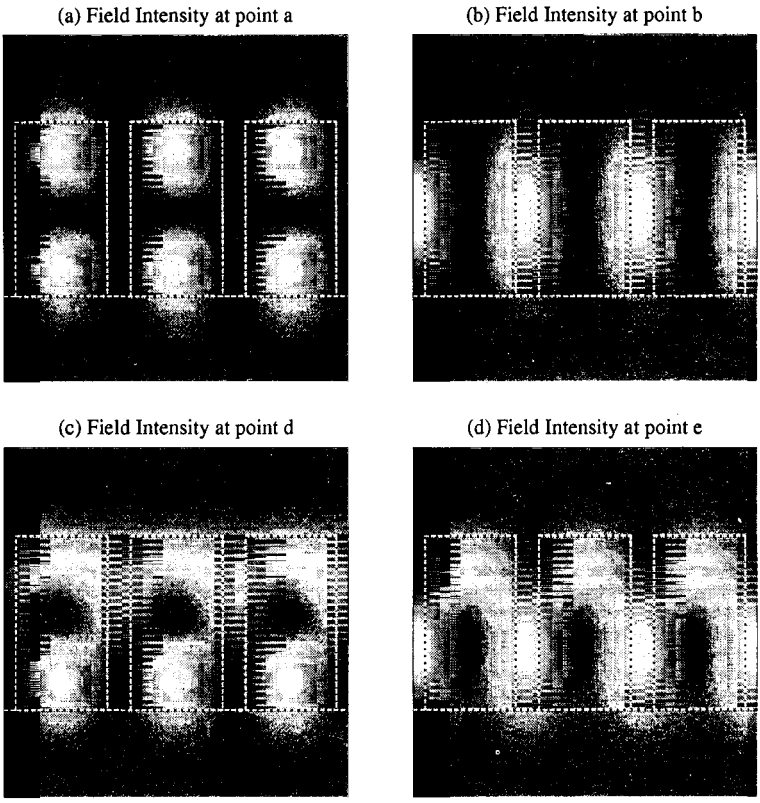

Figure 11. Field intensity distributions of selected TE guided Bloch modes at points a, b, d and e in figure 10. The substrate is below the horizontal dashed line and three periods of the high index waveguide layer are shown. (*a*) a first order slow mode, (*b*) a zero order fast mode, (*c*) a zero-group velocity slow 'mixed' mode and (*d*) a zero-group velocity fast 'mixed' mode.

8.4. *Microstructure of the fields*

Figure 11 shows the electric field intensity distribution of the TE guided Bloch modes at points a, b, d and e on figure 10. Figure 11 (*a*) shows the first order slow mode at point a. This is characteristically concentrated in the high index regions and has a double lobed structure in the z direction. The zero order fast mode (point b on figure 10) is shown in figure 11 (*b*); it is guided predominantly in the air gaps. This very unusual behaviour arises because the field pattern is below the resolution limit of free waves in the cover and substrate regions. The modes at points a and b have zero group velocity along the waveguide, as confirmed by the 100% visibility of the modal fringe pattern—no power can flow through regions where the fields are zero.

It is intriguing that four other points of zero group velocity occur, at anticrossing points on either side of the symmetrical point (e.g. d and e). The field intensity patterns of the modes at these points are given in figures 11 (*c*) and (*d*). It turns out the anticrossing is caused by the simultaneous resonance of the zero order fast and the first order slow modes, which are then coupled strongly together at the upper and lower boundaries (see figure 6), creating a stopband in β. Since they travel in opposite directions along the guide, a kind of 'tug-of-war' results between the fast and slow modes, giving rise to zero group velocity at the anticrossing point. The overall modal field distributions of these 'mixed' modes are superpositions of fast and slow modes, whose relative phase is such that constructive interference occurs near the substrate in both cases (d and e).

8.5. *Comparison with numerical analysis*

In order to confirm the accuracy of our simple analytical model, a numerical calculation was performed based on the method of Pendry and MacKinnon [17]. Our analytical model could be extended by generalization of (17) to include the contributions of higher order Fourier components and evanescent (imaginary β) solutions in the expansion of the field within the grating layer. In practice it is more efficient to recast the equations to relate the Fourier components in the cover to those in the substrate by means of a transfer matrix. The elements of this transfer matrix could be calculated by use of the dispersion relation (A9), the Fourier decomposition (12) and the matching conditions at the substrate and cover boundaries. In practice, due to its availability and flexibility, a finite difference algorithm, initiated by Pendry and MacKinnon, was used to calculate the transfer matrix. This works by discretizing the fields on a real space mesh and has the added advantage of being able to describe more complex grating geometries, such as V-grooves and two-dimensional periodicity. These structures will be considered in future papers.

The condition for appearance of a guided mode is that there be no unphysical exponentially diverging modes in the substrate and cover. This results in a determinantal equation, based on the transfer matrix, which is numerically solved. Table 1 shows a comparison of the resonant frequencies calculated at a number of points indicated on figure 10. The results for both methods correspond very well, close to the symmetric point the error is less than 0·5% and it increases to 3·16% when $k_y \Lambda/\pi$ is reduced to 0·5.

Table 1. Comparison of numerical and analytic models.

Point	$k_y\Lambda/\pi$	Numerical frequency ν	Analytic frequency ν	% error
a	1	3·78827	3·77557	0·33
b	1	3·62286	3·61706	0·16
c	1	2·9912	2·98968	0·05
d	0·91	3·72836	3·71371	0·39
e	0·91	3·71143	3·70417	0·20
f	0·91	2·90133	2·89861	0·09
g	0·75	3·44574	3·41174	0·99
h	0·5	2·88822	2·79708	3·16

9. Discussion

9.1. *Resonant tunnelling model*

A different and instructive analysis can quite easily be constructed based on resonant tunnelling (known as the tight-binding model in electronic band theory). Under the correct conditions, the fields in the air gaps between the high index lines are evanescent. This means that high index lines support guided modes that—under the appropriate conditions—bounce to and fro between substrate and cover. A single isolated line will support strongly confined resonances, the number being related to the thickness h of the layer. These are not perfectly confined because the plane wave spectrum (in the substrate and cover) of the field pattern created by an isolated resonator is continuous, containing wavevectors that carry energy into the cover and the substrate. In a *periodic* array of lines, however, the resonances are perfectly trapped; this is because the plane wave spectrum of a guided Bloch mode (close to the symmetrical points) consists of an infinite number of *discrete* spikes, and therefore contains *no* wavevectors that can leak into the cover or substrate. Note that the resonant tunnelling approach is not capable of predicting the fast modes guided in the air regions.

9.2. *Lifetime of localized state*

It is interesting to estimate the lifetime of a stationary mode at the symmetrical points. This will depend on the required physical length L_R of the excitation, since this determines the spectral spread Δk_y of in-plane wavevectors and hence the frequency spread $\Delta\nu$ needed; a shorter length L_R implies a larger Δk_y and vice versa. The edges of this spectrum reside on each side of the symmetrical points, and carry energy away from the resonance at a small but finite rate. Clearly, the flatter the curve on the ν versus k_y diagram, the less severe this leakage will be. For a Lorentzian distribution of amplitude $a_0(y)$ at $t = 0$, with Fourier transform $A(k_y)$:

$$a_0(y) = \frac{1}{1 + (y/b)^2}, \quad A(k_y) = \pi b \exp(-k_y b) \tag{20}$$

it is easy to show that, assuming a quadratic dependence of frequency ω on wavevector k_y close to the symmetrical point:

$$\omega(k_y) = \omega_0 - q(k_y^2 - k_{y0}^2) \tag{21}$$

(where ω_0 and k_{y0} are the values at the symmetrical point), that the time taken for the intensity at the peak to drop to one half is:

$$\tau_{1/2} = \frac{\pi b^2}{2q}. \tag{22}$$

For the symmetrical point, c in figure 10, at $v = 2{\cdot}990$, $q = 0{\cdot}027\ \mathrm{m^2\,s^{-1}}$ which yields a half life of 58 μs for $b = 1$ mm. Viewing the system as a resonator of period equal to the transit time substrate–cover–substrate, this gives a Q-factor of approximately 10^4. This of course neglects losses due to components in the modal k_y spectrum whose wavevectors are far enough from the symmetrical point to excite waves in the substrate and cover regions.

9.3. *Applications*

As is well known, placing a single atom in a high Q-factor single-mode micro-resonator whose frequency coincides with a radiative atomic transition will result in quantum electro-dynamical effects such as Rabi splitting [18]. Two different approaches may be used for producing high Q-factor micro-resonators in these etched films. The first exploits the zero group velocity at the symmetrical points, and has been discussed in section 9.2. In the second, a defect state is created within the in-plane momentum gap of the layer. This could be achieved by introducing a point defect in the form of a slightly thicker or thinner dielectric line. The state thus created will not, however, be perfectly trapped. This is because (as in section 9.2) its plane wave spectrum will contain wavevectors that can excite free waves in the substrate and cover regions, causing small but significant leakage and reducing the Q-factor.

The field microstructure of the slow mode at the symmetrical points has most of its energy concentrated in the high index regions, while the fast mode has most of its energy concentrated in the air gaps. It would make sense to exploit the fast mode as the basis of a gas sensor or even a gas laser; the zero group velocity would greatly enhance the atom–photon interaction and increase the sensitivity or the gain. The slow mode could be excited—as in the currently proposed arrays of vertical cavity emitting lasers—by introducing gain in the high index regions alone.

If the thickness of a conventional non-periodic waveguiding film is increased, then more modes are supported. In deeply etched periodic films, however, the presence of a substantial momentum gap acts to reduce the number of guided modes that would otherwise appear in a layer of the same average refractive index (see section 8.3). It may be possible to design a thick waveguide (multi-mode based on considerations of average index) in which all but the highest order mode are suppressed, rendering the structure single-mode [16]. This could have applications in single-frequency waveguide lasers where an increased single-mode volume would be beneficial.

Consider a layer thickness of $1{\cdot}5\Lambda$, for which a slow resonance exists at a normalized frequency of 2·990 (point c on figure 10); this corresponds to a vacuum wavelength of $6{\cdot}199\Lambda$. At a vacuum wavelength of 1550 nm this gives a grating period, $\Lambda = 250$ nm, the air gaps would have to be 50 nm ($0{\cdot}2\Lambda$) in length within a layer 375 nm thick. These feature sizes are within the capabilities of current semiconductor processing technology, as recently demonstrated by Krauss *et al.* [10].

10. Conclusions

Deeply etched high index films support two different types of fully guided Bloch modes with zero group velocities in the waveguide plane. Viewed as resonances, these stationary modes have a uniquely high effective Q-factor (compared to any of the other modes guided in the film) and hence are suitable as micro-resonators for ehancing dipole–field coupling. Although the analysis applies only to singly periodic layers, its general conclusions are relevant to the more general case of two-dimensional multiply periodic thin films, in which resonances that are stationary in all three space dimensions are feasible. The approach used may be helpful in future studies of the behaviour of arrays of vertical cavity surface emitting lasers.

Acknowledgments

The Optoelectronics Research Centre is an Interdisciplinary Research Centre of the United Kingdom Engineering and Physical Sciences Research Council (EPSRC). D. M. Atkin is the recipient of an EPSRC CASE award with the Defence Research Agency, Malvern.

Appendix: Translation matrix elements

The matrix $\mathbf{M}_{21}$ relating the field in the second layer to the field in the first layer is:

$$\begin{pmatrix} a_2^N \\ b_2^N \end{pmatrix} = \mathbf{M}_{21}\begin{pmatrix} a_1^N \\ b_1^N \end{pmatrix} = \begin{pmatrix} A_{21} & B_{21} \\ C_{21} & D_{21} \end{pmatrix}\begin{pmatrix} a_1^N \\ b_1^N \end{pmatrix}, \tag{A 1}$$

where

$$\begin{aligned} A_{21} &= c_1c_2 - (\xi_1p_1\Lambda/\xi_2p_2\Lambda)s_1s_2, \\ B_{21} &= s_1c_2/(\xi_1p_1\Lambda) + c_1s_2/(\xi_2p_2\Lambda), \\ C_{21} &= -\xi_1p_1\Lambda s_1c_2 - \xi_2p_2\Lambda c_1s_2, \\ D_{21} &= c_1c_2 - (\xi_2p_2\Lambda/\xi_1p_1\Lambda)s_1s_2, \end{aligned} \tag{A 2}$$

$$\det(\mathbf{M}_{21}) = 1,$$

where the terms s_j and c_j are shorthand for:

$$c_j = \cos(p_jh_j/2), \quad s_j = \sin(p_jh_j/2). \tag{A 3}$$

The matrix $\mathbf{M}_{12}$ relating the field in the first layer of the $(N+1)$th period to the field in the second layer of the Nth period is then

$$\begin{pmatrix} a_1^{N+1} \\ b_1^{N+1} \end{pmatrix} = \mathbf{M}_{12}\begin{pmatrix} a_2^N \\ b_2^N \end{pmatrix} = \begin{pmatrix} D_{21} & B_{21} \\ C_{21} & A_{21} \end{pmatrix}\begin{pmatrix} a_2^N \\ b_2^N \end{pmatrix}. \tag{A 4}$$

The analysis can either be based on the translation matrix $\mathbf{M} = \mathbf{M}_{12}\mathbf{M}_{21}$ (with a state vector representing the field in layers with index n_1) or equivalently on the matrix $\mathbf{M}' = \mathbf{M}_{21}\mathbf{M}_{12}$ (state vector representing the field in layers with index n_2). $\mathbf{M}$ is

$$\begin{pmatrix} a_1^{N+1} \\ b_1^{N+1} \end{pmatrix} = \mathbf{M}\begin{pmatrix} a_1^N \\ b_1^N \end{pmatrix} = \begin{pmatrix} A & B \\ C & D \end{pmatrix}\begin{pmatrix} a_1^N \\ b_1^N \end{pmatrix}, \tag{A 5}$$

where

$$A = D = A_{21}D_{21} + B_{21}C_{21}, \tag{A 6}$$

$$B = 2D_{21}B_{21}, \quad C = 2A_{21}C_{21}. \tag{A 7}$$

A can be re-arranged as

$$A = \cos(p_1h_1)\cos(p_2h_2) - \frac{1}{2}\left(\frac{p_1\xi_1}{p_2\xi_2} + \frac{p_2\xi_2}{p_1\xi_1}\right)\sin(p_1h_1)\sin(p_2h_2) \tag{A 8}$$

but B and C are most conveniently expressed as the product of two factors as above. The elements of the alternative matrix $\mathbf{M}'$ are:

$$A' = D' = A, \tag{A 9}$$

$$B' = 2A_{21}B_{21}, \quad C' = 2D_{21}C_{21}. \tag{A 10}$$

References

[1] See special issue: 1993, *J. opt. Soc. Am.* **B 10,** 283–407.
[2] See special issue: 1994, *J. mod. Optics*, **41,** 195–393.
[3] Joannopoulos, J., Meade, R. D., and Winn, J. N., 1995, *Photonic Crystals* (New York: Princeton).
[4] Yablonovitch, E., 1995, *Confined Electrons and Photons: New Physics and Applications*, edited by E. Burstein and C. Weisbuch (New York: Plenum Press).
[5] Gérard, J. M., Izrael, A., Marzin, J. Y., and Padjen, R., 1994, *Solid State Electron.*, **37,** 1341.
[6] Birks, T. A., Roberts, P. J., Russell, P. St. J., Atkin, D. M., and Shepherd, T. J., 1995, *Electron. Lett.*, **31,** 1941.
[7] Villeneuve, P. R., and Piché, M., 1992, *Phys. Rev. B*, **46,** 4649.
[8] Maradudin, A. A., and McGurn, A. R., 1994, *J. mod. Optics*, **41,** 275.
[9] Russell, P. St. J., Birks, T. A., and Lloyd-Lucas, F. D., 1995, *Confined Electrons and Photons: New Physics and Applications*, edited by E. Burstein and C. Weisbuch (New York: Plenum Press).
[10] Krauss, T., Song, Y. P., Thomas, S., Wilkinson, C. D. W., and DeLaRue, R. M., 1994, *Electron. Lett.*, **30,** 1444.
[11] Yamamoto, Y., and Slusher, R. E., 1993, *Phys. Today*, June, 66.
[12] Feng, X.-P., and Arakawa, Y., 1995, Conference on Lasers and Electro-Optics/Pacific Rim (Piscataway, Orlando: IEEE), paper TuL4.
[13] Yariv, A., 1991, *Optical Electronics*, Chap. 13 (Saunders College Publishing).
[14] Kogelnik, H., 1988 and 1990, *Guided-Wave Optoelectronics*, edited by T. Tamir (Berlin, Heidelberg: Springer-Verlag).
[15] Yeh, P., Yariv, A., and Hong, C. S., 1979, *J. opt. Soc. Am.*, **67,** 423.
[16] Atkin, D. M., Russell, P. St. J., Birks, T. A., and Roberts, P. J., 1995, *Conference on Lasers and Electro-Optics*, **15,** OSA Technical Digest Series (Washington, D.C.: Optical Society of America) p 223.
[17] Pendry, J. B., 1994, *J. mod. Optics*, **41,** 209.
[18] Houdré, R., Stanley, R. P., Oesterle, U., Ilegems, M., and Weisbuch, C., 1993, *J. Phys. IV Colloque*, **C5 3,** 51.